

# The roles of bulk and surface thermodynamics in the selective adsorption of a confined azeotropic mixture

Katie L. Y. Zhou,<sup>1</sup> Anna T. Bui,<sup>2,1</sup> and Stephen J. Cox<sup>1,\*</sup>

<sup>1</sup>Department of Chemistry, Durham University, South Road, Durham, DH1 3LE, United Kingdom

<sup>2</sup>Yusuf Hamied Department of Chemistry, University of Cambridge, Lensfield Road, Cambridge, CB2 1EW, United Kingdom

(Dated: January 30, 2026)

Fluid mixtures that exhibit an azeotrope cannot be purified by simple bulk distillation. Consequently, there is strong motivation to understand the behavior of azeotropic mixtures under confinement. We address this problem using a machine-learning-enhanced classical density functional theory applied to a binary Lennard-Jones mixture that exhibits azeotropic phase behavior. As proof-of-principle of a “train once, learn many” strategy, our approach combines a neural functional trained on a single-component repulsive reference system with a mean-field treatment of attractive interactions, derived within the framework of hyperdensity functional theory (hyper-DFT). The theory faithfully describes capillary condensation and results from grand canonical Monte Carlo simulations. Moreover, by taking advantage of a known accurate equation of state, the theory we present well-describes bulk thermodynamics by construction. Exploiting the computational efficiency of hyper-DFT, we systematically evaluate adsorption selectivity across a wide range of compositions, pressures, temperatures, and wall-fluid affinities. In cases where the wall-fluid interaction is the same for both species, we find that the pore becomes completely unselective at the bulk azeotropic composition. Strikingly, this unselective point persists far from liquid-vapor coexistence, including in the supercritical regime. Analysis of the bulk equation of state across a wide range of thermodynamic state points shows that the azeotropic composition coincides with equal partial molar volumes and an extremum in the isothermal compressibility. A complementary thermodynamic analysis demonstrates that unselective adsorption corresponds to an azeotrope (a point of zero relative adsorption) and an extremum in the interfacial free energy. We also find that the two interfaces of the slit pore behave independently down to remarkably small slits.

## I. INTRODUCTION

A detailed understanding of the thermophysical properties of fluid mixtures under confinement is crucial for a wide range of applications, including industrial separation processes, gas storage, and healthcare [1–3]. Specific examples span oil recovery [4], hydrogen storage [5, 6], and microfluidic systems [7, 8]. From a theoretical standpoint, molecular simulations are widely regarded as the method of choice [9–14], offering microscopic insight that is often inaccessible to experiment alone [15, 16]. However, traditional approaches rooted in liquid state theory are experiencing a renaissance [17, 18]. In particular, classical density functional theory (cDFT) is attracting renewed interest in physical chemistry, driven by the ability of machine learning (ML) to deliver highly accurate and computationally efficient approximations [19–27].

In this article, our aim is to demonstrate a recently proposed ML-based approach to cDFT for a simple Lennard-Jones (LJ) fluid mixture. While similar ideas have been explored recently in Ref. 21, our approach differs in two key respects. First, methodologically, we train the ML model on a repulsive *single-component* reference system and incorporate attractive interactions through a simple mean-field treatment—an approach that enhances transferability among systems. Second, from an application standpoint, we focus on a binary mixture with asymmetric interactions,

which exhibits azeotropic phase behavior. As we will see, the existence of an azeotrope appears to strongly influence the fluid’s behavior—both in bulk and under confinement—across a broad range of thermodynamic conditions.

The potential appeal of cDFT over molecular simulations becomes immediately evident when considering its fundamental formalism [28, 29]. The central object in cDFT is the grand potential functional

$$\Omega_V([\{\varrho_\alpha\}], T) = \mathcal{F}_{\text{intr}}^{(\text{id})}([\{\varrho_\alpha\}], T) + \mathcal{F}_{\text{intr}}^{(\text{ex})}([\{\varrho_\alpha\}], T) + \sum_\alpha \int d\mathbf{r} \varrho_\alpha(\mathbf{r}) [V_\alpha(\mathbf{r}) - \mu_\alpha], \quad (1)$$

where  $\mathcal{F}_{\text{intr}}^{(\text{id})}$  and  $\mathcal{F}_{\text{intr}}^{(\text{ex})}$  are, respectively, the ideal and excess intrinsic Helmholtz free energy functionals. A particle of species  $\alpha$ , with chemical potential  $\mu_\alpha$ , experiences an external one-body potential  $V_\alpha$ , while  $\varrho_\alpha$  denotes its average one-body density, though not necessarily at equilibrium. Functional minimization of  $\Omega_V$  with respect to  $\varrho_\alpha$  yields the equilibrium one-body density of species  $\alpha$ ,  $\rho_\alpha$ , which satisfies the Euler–Lagrange equation,

$$\Lambda_\alpha^3 \rho_\alpha(\mathbf{r}) = \exp \left( -\beta [V_\alpha(\mathbf{r}) - \mu_\alpha] + c_\alpha^{(1)}(\mathbf{r}; [\{\rho_\alpha\}], T) \right) \quad (2)$$

with  $\Lambda_\alpha$  denoting the thermal de Broglie wavelength of species  $\alpha$ ,  $\beta = 1/k_B T$  ( $k_B$  is the Boltzmann constant), and

$$c_\alpha^{(1)}(\mathbf{r}; [\{\rho_\alpha\}], T) = -\frac{\delta \beta \mathcal{F}_{\text{intr}}^{(\text{ex})}([\{\varrho_\alpha\}], T)}{\delta \varrho_\alpha(\mathbf{r})}, \quad (3)$$

\* stephen.j.cox@durham.ac.uk

is the one-body direct correlation functional. In the context of the Euler–Lagrange equation,  $c_\alpha^{(1)}$  acts as a self-consistent one-body potential that accounts for the effects of correlations on the structure of the fluid. With the equilibrium densities from Eq. 2, the grand potential of the system readily follows:  $\Omega = \Omega_V([\{\rho_\alpha\}], T)$ . The procedure for obtaining the structure and thermodynamics of the system can, therefore, be succinctly put: minimize a functional to obtain the equilibrium structure, then evaluate the functional at equilibrium to obtain the thermodynamic potential of the system. This is a far simpler operation than explicitly sampling the many-body equilibrium distribution function with molecular simulations.

What, then, has prevented cDFT from becoming the method of choice for understanding the equilibrium properties of fluids? The answer is straightforward. While a rigorous theoretical framework, in practice cDFT relies upon approximations to  $\mathcal{F}_{\text{intr}}^{(\text{ex})}$ . (Only for hard rods in a single dimension is  $\mathcal{F}_{\text{intr}}^{(\text{ex})}$  known exactly [30].) In the case of hard spheres, very good approximations founded on Rosenfeld’s fundamental measure theory (FMT) have been available for several decades [31–34]. When combined with an *ad hoc* mean-field treatment of attractive interactions, cDFT has been shown to be a powerful practical method for understanding the physics of simple liquids. In particular, the physics of capillarity [35, 36], surface drying and wetting [37, 38], and solvophobicity [39] have been extensively studied in single-component systems, owing to the ability of the mean-field approximation to qualitatively capture liquid–gas phase coexistence. While less intensely studied compared to single-component fluids, such a mean-field approach has also provided qualitative insight into the behavior of simple mixtures [40–47], though the richer phase behavior of multicomponent fluids—including liquid–liquid coexistence, azeotropy and heteroazeotropy [48]—pushes the limits of analytical approximations for  $\mathcal{F}_{\text{intr}}^{(\text{ex})}$ .

Going beyond hard spheres and a mean-field treatment for attractive interactions has, however, proven a major challenge. Naturally, several groups have recently turned to ML. For example, early works by Oettel and co-workers focused on one-dimensional systems [27, 49] and anisotropic patchy particles [50], while Cats *et al.* used ML to improve the standard mean-field approximation for the three-dimensional LJ fluid [25]. One ML scheme that is gaining significant traction is “neural functional theory” [19] introduced by Sammüller *et al.* The basis of this physics-informed approach is the Euler–Lagrange equation (Eq. 2). For known  $\{V_\alpha\}$  and  $\{\mu_\alpha\}$ , with  $\{\rho_\alpha\}$  obtained from grand canonical Monte Carlo (GCMC) simulation,  $\{c_\alpha^{(1)}\}$  at equilibrium are determined by rearranging Eq. 2:

$$c_\alpha^{(1)}(\mathbf{r}; [\{\rho_\alpha\}], T) = \ln \Lambda_\alpha^3 \rho_\alpha(\mathbf{r}) + \beta(V_\alpha(\mathbf{r}) - \mu_\alpha). \quad (4)$$

By obtaining  $\{c_\alpha^{(1)}\}$  from many different GCMC simulations with different  $\{V_\alpha\}$  and  $\{\mu_\alpha\}$ , a training set is established to learn the local functional dependence of  $c_\alpha^{(1)}$  on  $\{\rho_\alpha\}$  with a neural network.

Originally developed for the single-component hard-sphere fluid—where it even outperformed FMT-based functionals [19]—the neural cDFT approach has since been extended to more complex systems. For example, Sammüller *et al.* applied neural cDFT to the LJ fluid, demonstrating accurate predictions of liquid–vapor coexistence [22]. Building on this, Robitscko *et al.* showed that liquid–liquid coexistence in a simple binary LJ mixture is also well captured [21]. By incorporating orientational correlations, Yang *et al.* have successfully applied neural cDFT to molecular CO<sub>2</sub> [26].

While neural cDFT exploits the local nature of correlations, Bui and Cox addressed systems with long-ranged electrostatic interactions [20], combining neural cDFT with a systematically improvable mean-field approach inspired by local molecular field theory (LMFT) [51]. Initially developed for primitive electrolyte models [20], this LMFT-style framework was later generalized to systems with nontrivial coupling between charge and number density, such as polar fluids [23, 52]. At the foundation of this generalization lies hyperdensity functional theory [53] (hyper-DFT), also introduced by Sammüller *et al.* in the context of soft matter, which establishes that any equilibrium observable can be expressed as a functional of the one-body density. Leveraging hyper-DFT, Bui and Cox established a rigorous framework for electromechanics in fluids [52] and demonstrated that electric field gradients can alter liquid–vapor coexistence in polar fluids, including water [23]. This work uncovered a previously unknown effect—dielectrocapillarity—in which field gradients control adsorption into porous media.

Clearly, the neural functional approach offers a route to fully harness the advantages of cDFT over molecular simulations. While the LMFT-style hyper-DFT arguably remains essential for systems dominated by long-range interactions, many systems can now be tackled simply by learning  $\{c_\alpha^{(1)}\}$ , without invoking any of the standard approximations of liquid-state theory. In this light, can traditional strategies—such as decomposing the system into a repulsive reference plus mean-field attraction, as in FMT-based approaches—still play a meaningful role?

We argue that the answer is “yes.” Our reasons are twofold. First, when the bulk equation of state (EoS) is well established by other means, the hyper-DFT mean-field framework described in Ref. 52 offers a straightforward way to leverage the rich information that it encodes. By adopting this strategy, we can focus efforts where they are most needed: neural cDFT can be targeted to the study of inhomogeneous systems where its advantages are most pronounced, leaving the bulk physics to the already-known EoS. Second, while cDFT itself is more efficient than molecular simulations, neural cDFT comes with an initial computational overhead in obtaining the training data. Decomposing the system into a repulsive reference—treated with neural cDFT—and mean-field attractive interactions, opens the door to a “train once, learn many” strategy, where a single, accurate repulsive reference can be reused across multiple systems. Such an approach becomes particularly advantageous in the case of mixtures; in this article, we demonstrate

a proof-of-principle for a binary LJ mixture with asymmetric interactions that exhibits azeotropy.

The rest of the article is organized as follows. In Sec. II, we introduce the LJ mixture and outline the underpinning hyper-DFT framework. In Sec. III, we validate the approach against GCMC simulations and examine adsorption and selectivity in a slit-pore that interacts with both species in the same manner. We analyze the bulk thermodynamic behavior of the mixture, with particular emphasis on the role of the azeotropic composition across a wide range of pressures and temperatures, in Sec. IV. In Sec. V, we develop a thermodynamic description of pore selectivity that sheds light on the underlying driving forces for selective adsorption. Finally, Sec. VI summarizes our main findings and discusses their broader implications and possible extensions.

## II. MEAN-FIELD NEURAL HYPER-DFT SUCCESSFULLY DESCRIBES AN ASYMMETRIC BINARY LJ MIXTURE

The intermolecular interactions that govern fluid mixtures can, in general, be complicated, potentially comprising strongly directional interactions in the form of hydrogen bonds [54], long-ranged electrostatic effects [55, 56], and even metallicity [57]. Nonetheless, many of the most salient aspects of fluid mixtures are captured by relatively simple forms for the intermolecular interactions. For instance, complex liquid–vapor and liquid–liquid phase equilibria are reproduced with LJ mixtures [58, 59], alkane phase separation with generalized Mie potentials [60], binary alloys with Stillinger–Weber [61, 62] and Tersoff [63, 64] potentials, and polymer demixing with Gaussian core models [65].

Here, the system we investigate is a binary mixture of species A and B, whose pairwise interactions are prescribed by the truncated and shifted LJ pair potential,

$$u_{\alpha\eta}(r) = \begin{cases} 4\epsilon_{\alpha\eta}[(\sigma/r)^{12} - (\sigma/r)^6], & r < r_c, \\ 0, & r \geq r_c, \end{cases} \quad (5)$$

where  $\alpha$  and  $\eta$  are species labels,  $r_c = 2.5\sigma$ , and the molecular diameter,  $\sigma$ , is the same for all particles. In contrast, the strength of interaction between particles is species-dependent. Specifically,  $\epsilon_{AA} = \epsilon$ ,  $\epsilon_{BB} = 0.9\epsilon$ , and  $\epsilon_{AB} = 0.806\epsilon$ . In Fig. 1a we present the predicted bulk phase diagram from the PETs EoS [66, 67] at a temperature  $k_B T/\epsilon = 0.77$ , in the  $P$ – $x_B$  plane, where  $P$  is pressure and  $x_B$  is the mole fraction of B. Previous studies [58, 59, 68] have shown that, at this temperature, this system exhibits a positive azeotrope—the point on the phase diagram at which liquid and vapor have the same composition—at mole fraction  $x_B^{(az)} \approx 0.67$  and pressure  $P^{(az)}\sigma^3/\epsilon = 0.0248$ .

To describe the structure and thermodynamics of this system in a density functional framework, we will adopt a hyper-DFT approach [53] rather than the traditional cDFT prescribed by Eqs. 1–3. In brief, the basis of hyper-DFT is an extended ensemble approach, which in this context

amounts to modifying the external potential operators,

$$\hat{\mathcal{V}}_\alpha(\mathbf{r}^{N_\alpha}) = \sum_i^{N_\alpha} V_\alpha(\mathbf{r}_i) + \sum_i^{N_\alpha} \phi_\alpha(\mathbf{r}_i), \quad (6)$$

where the summations are understood to be restricted to species  $\alpha$ . The effects of the additional external potentials  $\{\phi_\alpha\}$  are incorporated as an additional functional dependence on the excess intrinsic Helmholtz free energy functional,

$$\mathcal{F}_{\text{intr}}^{(\text{ex})}([\{\rho_\alpha\}], T) \rightarrow \mathcal{F}_{\text{intr}}^{(\text{ex})}([\{\rho_\alpha\}, \{\beta\varphi_\alpha\}], T),$$

and the set of one-body density functionals is introduced, e.g.,

$$\rho_\alpha^{(1)}(\mathbf{r}; [\{\rho_\alpha\}, \{\beta\varphi_\alpha\}], T) = \frac{\delta\beta\mathcal{F}_{\text{intr}}^{(\text{ex})}}{\delta\beta\varphi_\alpha(\mathbf{r})}. \quad (7)$$

At equilibrium, these one-body density functionals satisfy  $\rho_\alpha(\mathbf{r}) = \rho_\alpha^{(1)}(\mathbf{r}; [\{\rho_\alpha\}, 0], T)$ . We refer the reader to Ref. 69 for a more detailed discussion of the foundations of hyper-DFT.

For our current purpose, we have introduced hyper-DFT in order to systematically derive a mean-field treatment for attractive interactions, in the same spirit as LMFT developed by Weeks and co-workers [70–72]. To this end, we introduce a short-ranged reference system, with pairwise interactions  $u_{0,\alpha\eta}(r)$ . For this reference system, we seek the set of one-body potentials  $\{\phi_{R,\alpha}\}$  such that the resulting equilibrium one-body densities satisfy  $\rho_{R,\alpha}(\mathbf{r}) = \rho_\alpha(\mathbf{r})$  for all  $\alpha$ , where the subscript ‘R’ indicates properties pertaining to the reference system.

As shown in Appendix A of Ref. 52, but generalized here for mixtures, a pragmatic way to obtain  $\{\phi_{R,\alpha}\}$  is to assert a mean-field approximation,

$$\begin{aligned} \mathcal{F}_{\text{intr}}^{(\text{ex})}([\cdot], T) &= \mathcal{F}_{\text{intr},R}^{(\text{ex})}([\cdot], T) + \sum_\alpha \Delta\mu_\alpha \int d\mathbf{r} \rho_\alpha(\mathbf{r}) \\ &+ \frac{1}{2} \sum_{\alpha\eta} \int d\mathbf{r} \int d\mathbf{r}' \delta_u \rho_{R,\alpha}^{(1)}(\mathbf{r}; [\cdot], T) u_{1,\alpha\eta}(|\mathbf{r} - \mathbf{r}'|) \delta_u \rho_{R,\eta}^{(1)}(\mathbf{r}'; [\cdot], T), \end{aligned} \quad (8)$$

where  $\Delta\mu_\alpha = \mu_\alpha - \mu_{R,\alpha}$  is the difference in chemical potentials between the LJ and reference systems,  $u_{1,\alpha\eta} = u_{\alpha\eta} - u_{0,\alpha\eta}$ , and  $\delta_u \rho_{R,\alpha}^{(1)} = \rho_{R,\alpha}^{(1)} - \bar{\rho}_{R,\alpha}$ , with  $\bar{\rho}_{R,\alpha}$  denoting the uniform bulk density for species  $\alpha$  of the reference system.  $([\cdot])$  has been used as a shorthand notation for  $[\{\rho_\alpha\}, \{\beta\varphi_\alpha\}]$ .

By setting  $\{\phi_\alpha = 0\}$ , following Ref. 52, one can show that

$$\begin{aligned} c_\alpha^{(1)}(\mathbf{r}; [\{\rho_\alpha\}, 0], T) &= \\ c_{R,\alpha}^{(1)}(\mathbf{r}; [\{\rho_\alpha\}, 0], T) - \beta\phi_{R,\alpha}(\mathbf{r}) - \beta\Delta\mu_\alpha, \end{aligned} \quad (9)$$

where

$$\phi_{R,\alpha}(\mathbf{r}) = \sum_\eta \int d\mathbf{r}' u_{1,\alpha\eta}(|\mathbf{r} - \mathbf{r}'|) \delta_u \rho_{R,\eta}^{(1)}(\mathbf{r}'; [\{\rho_\alpha\}, 0], T). \quad (10)$$

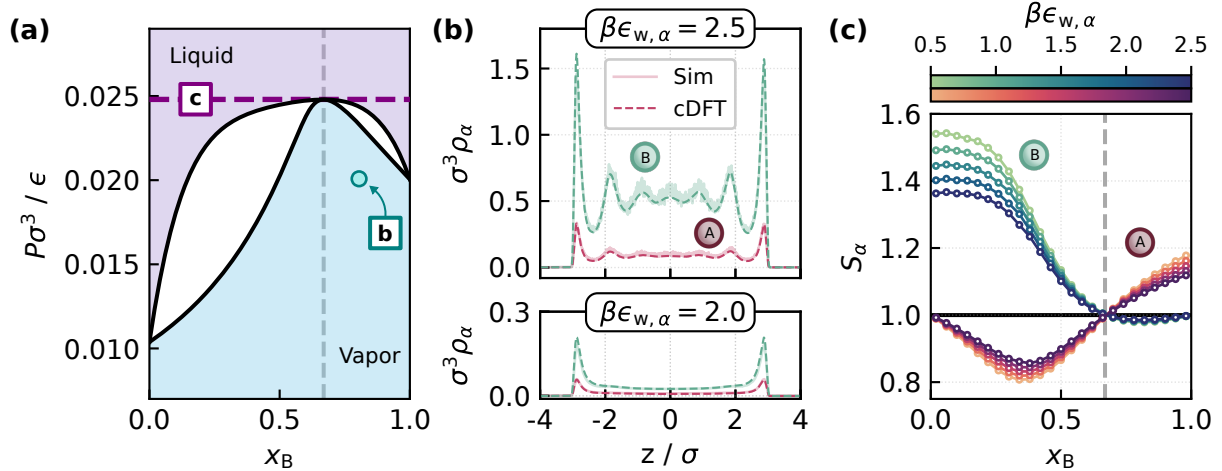


**Figure 1:** Effects of confinement on a binary LJ mixture. (a) The pressure-composition phase diagram of the mixture at  $k_B T / \epsilon = 0.77$ . An azeotrope forms at  $x_B^{(az)} \approx 0.67$ , as indicated by the vertical dashed line. The circle indicates the state point of the density profiles in (b), where the mixture is confined in a slit, for two different wall–fluid interaction strengths (as indicated by the labels). Good agreement between the theory and the simulation data is observed. (c) Pore selectivities vs  $x_B$  for different wall–fluid interactions, both for component A (orange to purple) and B (green to blue) at the azeotropic pressure, marked by the horizontal dashed line in (a). Lines serve as a guide to the eye. A reversal in selectivity is observed at  $x_B^{(az)}$ , as indicated by the vertical dashed line.

The hyper-DFT formulation of LMFT that we present is largely similar to that of Archer and Evans [73], who showed the formal similarity of LMFT and traditional cDFT. A key difference, however, is that in writing Eq. 8, we have separated the bulk and inhomogeneous contributions to the mean-field free energy functional. This separation affords a level of flexibility that can be put to practical advantage; an accurate description of the bulk fluid can be obtained if  $\{\Delta\mu_\alpha\}$  is known by any means. For example, in the case of primitive models of electrolytes and dielectric fluids, analytic expressions for  $\{\Delta\mu_\alpha\}$  have been derived based on Stillinger–Lovett sum rules [20, 52]. Here, we will take advantage of the fact that  $\{\Delta\mu_\alpha\}$  can be obtained from a known EoS.

Success of this LMFT-style hyper-DFT approach rests upon a suitable choice of reference system. For the binary LJ mixture that we study here, in which A and B have the same molecular diameter, we choose the reference system to be the purely repulsive *single-component* fluid described by the Weeks–Chandler–Anderson (WCA) potential [74], i.e.,  $u_{0,\alpha\eta} = u_0$ , with

$$u_0(r) = \begin{cases} 4\epsilon[(\sigma/r)^{12} - (\sigma/r)^6] + \epsilon, & r < 2^{1/6}\sigma \\ 0, & r \geq 2^{1/6}\sigma. \end{cases} \quad (11)$$

Combining Eqs. 2 and 9, the Euler–Lagrange equation for species  $\alpha$  of the LJ mixture reads,

$$\Lambda_\alpha^3 \rho_\alpha(\mathbf{r}) = \quad (12)$$

$$\exp(-\beta[V_\alpha(\mathbf{r}) + \phi_{R,\alpha}(\mathbf{r}) - \mu_{R,\alpha}]) + c_R^{(1)}(\mathbf{r}; [\bar{\rho}_A + \bar{\rho}_B], T)),$$

with

$$\mu_{R,\alpha}(\bar{\rho}_A, \bar{\rho}_B) = k_B T \ln \Lambda_\alpha^3 \bar{\rho}_\alpha - k_B T c_R^{(1)}([\bar{\rho}_A + \bar{\rho}_B], T). \quad (13)$$

Following Ref. 19, and detailed further in *Methods*, we trained a neural functional to represent  $c_R^{(1)}$  of the WCA fluid, using data from 900 GCMC simulations at temperatures  $k_B T / \epsilon = 1.0, 1.5$  and  $2.0$ . To evaluate the grand potential of the binary LJ mixture, we use Eqs. 1 and 8, with  $\mathcal{F}_{\text{intr},R}^{(\text{ex})}$  obtained by functional line integration [19], and  $\mu_\alpha(\bar{\rho}_A, \bar{\rho}_B)$  directly from the PeTS EoS [66]. In practice, the neural functional is limited to a planar geometry, i.e.,  $c_R^{(1)}(\mathbf{r}, [\{\rho_\alpha\}, T]) \rightarrow c_R^{(1)}(z, [\{\rho_\alpha\}, T])$ ; we direct the reader toward Ref. 75 for recent developments that extend the neural functional approach to resolution in higher dimensions.

In Fig. 1b we show results from this LMFT-style hyper-DFT for the binary LJ mixture in a slit-pore at equilibrium with a reservoir at  $k_B T / \epsilon = 0.77$ ,  $P\sigma^3 / \epsilon = 0.020$ , and  $x_B = 0.78$ , which corresponds to the vapor state. In these calculations, the left and right walls of the slit-pore each act as an external potential confining the particles to a region  $-L/2 < z < L/2$

$$V_\alpha^{(\text{single})}(z) = 4\epsilon_{w,\alpha} \left[ (\sigma/(z - z_w))^{12} - (\sigma/(z - z_w))^6 \right], \quad (14)$$

where  $z_w = \pm L/2$ . Similar to the interatomic potential, each  $V_\alpha^{(\text{single})}$  is truncated and shifted at a cutoff  $z_c = 2.5\sigma$ . In Fig. 1b, we have considered the symmetric case,  $\epsilon_{w,A} = \epsilon_{w,B} = 2.0 k_B T$ . For a mildly attractive interaction between the confining walls and the particles, equilibrium densities predicted from our LMFT-style neural hyper-DFT calculations are in excellent agreement with GCMC simulations, and overall consistent with a vapor-like state in the pore. Upon increasing the interaction strength to  $2.5 k_B T$ , hyper-DFT captures the transition to a liquid-like state predicted by GCMC simulations. While some minor discrepancies in the density profiles are observed for these more attractive

walls, agreement between theory and simulation remains very good.

Overall, the combination of the accurate PeTS EoS for bulk, and the neural functional for the inhomogeneous correlations means that our hyper-DFT approach outperforms the standard mean-field cDFT treatment across a broad range of thermodynamic conditions (see Figs. S1–S3). Moreover, we also demonstrate the robustness of our approach on other LJ binary mixtures with different attractive interactions, illustrating the potential power of the “train once, learn many” strategy (see Fig. S4).

### III. EFFICIENT EVALUATION OF PORE SELECTIVITY UNVEILS A SIGNIFICANCE OF THE AZEOTROPIC COMPOSITION UNDER CONFINEMENT

Having established the accuracy of our hyper-DFT approach, we now capitalize on its advantages as a density functional framework. Specifically, we investigate how confinement influences the overall composition of the fluid across a broad range of wall–fluid interaction strengths and thermodynamic conditions; this is especially important for systems that exhibit azeotropy, such as the binary LJ mixture under investigation here. While thermodynamic modeling of bulk mixtures is well-established [77], major gaps remain in our understanding of azeotropy under confinement (“adsorption azeotropy” [78–81])—addressing this issue is of broad relevance to chemical separation and industrial processes [82, 83].

To assess the influence of confinement on the composition of the fluid, we use hyper-DFT to compute the pore selectivity of each species [11, 44, 45, 84],

$$S_\alpha = \frac{N_\alpha / (N_A + N_B)}{x_\alpha}, \quad (15)$$

where  $N_\alpha$  is the total number of adsorbed particles of species  $\alpha$ ,

$$N_\alpha = \mathcal{A} \int_{-L/2}^{+L/2} dz \rho_\alpha(z), \quad (16)$$

and  $\mathcal{A}$  is the cross-sectional area of the slit pore. Note that  $x_\alpha$  is a property of the bulk reservoir. In the first instance, we evaluate  $S_\alpha$  at fixed  $T$  and  $P$  over a wide range of  $\epsilon_{w,A} = \epsilon_{w,B}$  and  $x_B$ , as shown in Fig. 1c.

Our calculations of  $S_\alpha$  reveal that, relative to the bulk composition, species B is preferentially adsorbed at low  $x_B$ , whereas species A is preferred at high  $x_B$ . This observation is consistent with previous studies that have found selective adsorption for the component with weaker fluid–fluid interactions when it is the minority component in bulk [43, 85]. The most striking observation from Fig. 1c, however, is that the crossover between B- and A-selectivity, where  $S_A = S_B = 1$ , occurs very close to the azeotropic composition, irrespective of the wall–fluid interaction strength; for reasons that will become clear in Sec. V, we refer to

this composition,  $x^{(an)}$ , as the “aneotropic composition” [86–88].

The fact that  $x_B^{(an)} \approx x_B^{(az)}$  appears insensitive to the strength of the wall–fluid interaction motivates us to investigate the extent to which the azeotropic composition influences pore selectivity under different thermodynamic conditions. To this end, we repeat our calculations at the same temperature  $k_B T / \epsilon = 0.77$  but at both higher and lower pressures, and again at  $k_B T / \epsilon = 1.50$ , with the results shown in Fig. 2a. The state points considered encompass regions both below and above the azeotropic and critical lines of the mixture on the  $P$ – $T$  phase diagram, as marked in Fig. 2b. Remarkably, all show the same crossover at  $x_B^{(an)} \approx x_B^{(az)}$ , despite being far from the azeotropic line.

So far, we have investigated slit pores that interact with species A and B in an identical fashion. Yet, even in this simple symmetric case, we observe selective adsorption. Moreover, we observe completely unselective behavior close to the azeotropic composition of the *bulk* fluid. Before going on to investigate how pore selectivity may vary in the case of asymmetric wall–fluid interactions, we therefore aim to understand the behavior of the bulk fluid in greater detail.

### IV. BULK THERMODYNAMICS AND THE ROBUST SIGNATURE OF AZEOTROPY

The results we present in Figs. 1c and 2 indicate that the azeotropic composition remains relevant to the mixture’s adsorption behavior even at thermodynamic conditions far from liquid–vapor coexistence. To shed light on these observations, we recall that the azeotrope is defined as the point of liquid–vapor coexistence at which composition of the two phases in bulk is the same:  $x_B^{(l)} = x_B^{(v)} = x_B^{(az)}$ , where the superscripts “(l)” and “(v)” indicate quantities that pertain to the liquid and vapor phases, respectively. Therefore, in addition to mechanical and thermal equilibrium, we have [48]

$$\mu_B^{(l)}(x_B^{(az)}, P^{(az)}, T^{(az)}) = \mu_B^{(v)}(x_B^{(az)}, P^{(az)}, T^{(az)}), \quad (17a)$$

$$\mu_A^{(l)}(x_B^{(az)}, P^{(az)}, T^{(az)}) = \mu_A^{(v)}(x_B^{(az)}, P^{(az)}, T^{(az)}), \quad (17b)$$

where,  $T^{(az)}$  and  $P^{(az)}$  are the temperature and pressure along the azeotropic line [76] in the  $P$ – $T$  plane (see Fig. 2b). Introducing the exchange potential,

$$\Delta_E \mu(x_B, P, T) = \mu_B(x_B, P, T) - \mu_A(x_B, P, T), \quad (18)$$

and subtracting Eq. 17b from Eq. 17a, we find

$$\Delta_E \mu^{(l)}(x_B^{(az)}, P^{(az)}, T^{(az)}) = \Delta_E \mu^{(v)}(x_B^{(az)}, P^{(az)}, T^{(az)}). \quad (19)$$

Thus, under azeotropic conditions, the reversible work required to exchange a particle of species A for one of species B, as encoded in  $\Delta_E \mu$ , is identical in the liquid and vapor phases.

Inspired by the observation that the azeotropic composition appears relevant across a broad range of  $P$  and  $T$ ,

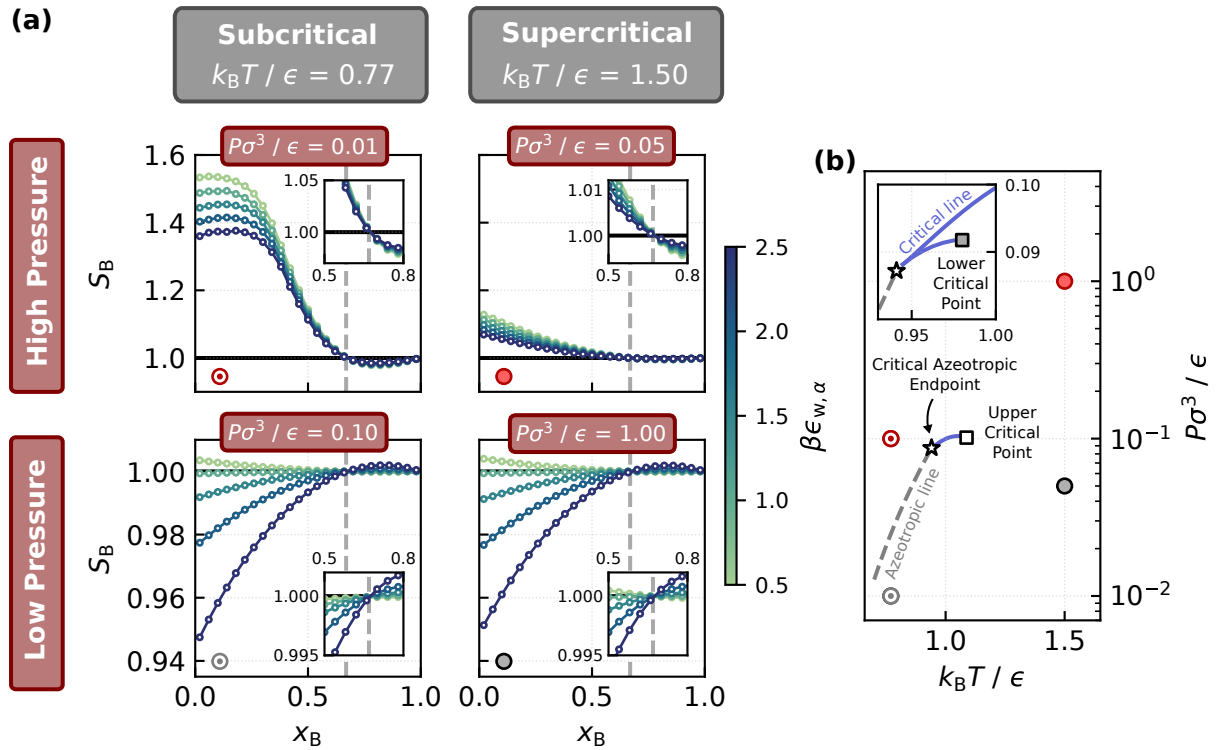


**Figure 2:** The relevance of the azeotropic composition across a broad range of thermodynamic conditions. (a)  $S_B$  vs  $x_B$  with varying wall-fluid interaction strengths at different state points, as indicated by the labels. The top and bottom panels correspond to liquid and vapor, respectively, in the reservoir. In all cases, a crossover in selectivity occurs at  $x_B \approx x_B^{(az)}$ . (b)  $P$ - $T$  phase diagram, with the thermodynamic state points used in (a) marked by the circles. The critical azeotropic endpoint is  $k_B T_{CAEP}/\epsilon \approx 0.94$  [76] (star) and the upper critical point is  $k_B T_C/\epsilon \approx 1.09$  (white square). The inset shows the region around  $k_B T_{CAEP}/\epsilon$  with the lower critical point.

we investigate the behavior of the exchange potential away from coexistence. To this end, in Fig. 3a we show how  $\Delta_E\mu$  varies with  $x_B$  for different  $P$  and  $T$ . At subcritical temperatures, we see that  $\Delta_E\mu(x_B)$  obtained at different pressures collapse into two distinct branches, corresponding to the vapor and liquid states. Strikingly, we observe that these two branches cross at  $x_B^{(az)}$ . At supercritical temperatures, while no longer separated into liquid and vapor branches, the observation that  $\Delta_E\mu(x_B^{(az)})$  is equal for all  $P$  persists. This observation implies that,

$$\left( \frac{\partial \Delta_E\mu}{\partial P} \right)_{x_B=x_B^{(az)}, T} = 0, \quad (20)$$

for all  $T$  investigated. An alternative, but equivalent, viewpoint is that at the azeotropic composition, irrespective of  $P$  and  $T$ , the partial molar volumes,  $\tilde{v}_\alpha = (\partial\mu_\alpha/\partial P)_{x,T}$ , of A and B are identical.

For single component fluids, there has been much interest in characterizing the nature of the supercritical state. In particular, while the critical point is defined by the indistinguishability of liquid and vapor states, several studies suggest regions in the phase diagram—often separated by so called “Widom lines”—where the supercritical state behaves more liquid- or vapor-like [89–94]. To our knowledge, the supercritical state of binary fluids remains much less in-

tensely studied [95, 96]. In this context, the observation of identical partial molar volumes at  $x_B^{(az)}$  at  $T \gg T_c$  is intriguing. While an exhaustive study into this topic remains beyond the scope of this article, in Fig. 3b we show how the isothermal compressibility,

$$\chi_T(x_B, P, T) = \frac{1}{\bar{\rho}} \left( \frac{\partial \bar{\rho}}{\partial P} \right)_{x_B, T}, \quad (21)$$

where  $\bar{\rho} = \bar{\rho}_A + \bar{\rho}_B$ , varies with  $x_B$  for different  $P$  and  $T$ . Though not unique, locating conditions of maximum isothermal compressibility is a common approach to mapping Widom lines in single-component systems [89–94]. For the binary system we consider, we see that  $\chi_T(x_B^{(az)}, P, T)$  is locally extremum. Specifically, at subcritical temperatures, we observe that vapor and liquid states are characterized by positive and negative curvatures, respectively. Remarkably, hallmarks of this observation persist at supercritical temperatures, with  $\chi_T(x_B^{(az)}, P, T)$  a local minimum at low pressures, and a local maximum at high pressures. For now, we leave this as an intriguing observation. Our initial results for pore selectivity (Figs. 1c and 2), however, hint that such supercritical behavior of the bulk fluid influences behavior under confinement.

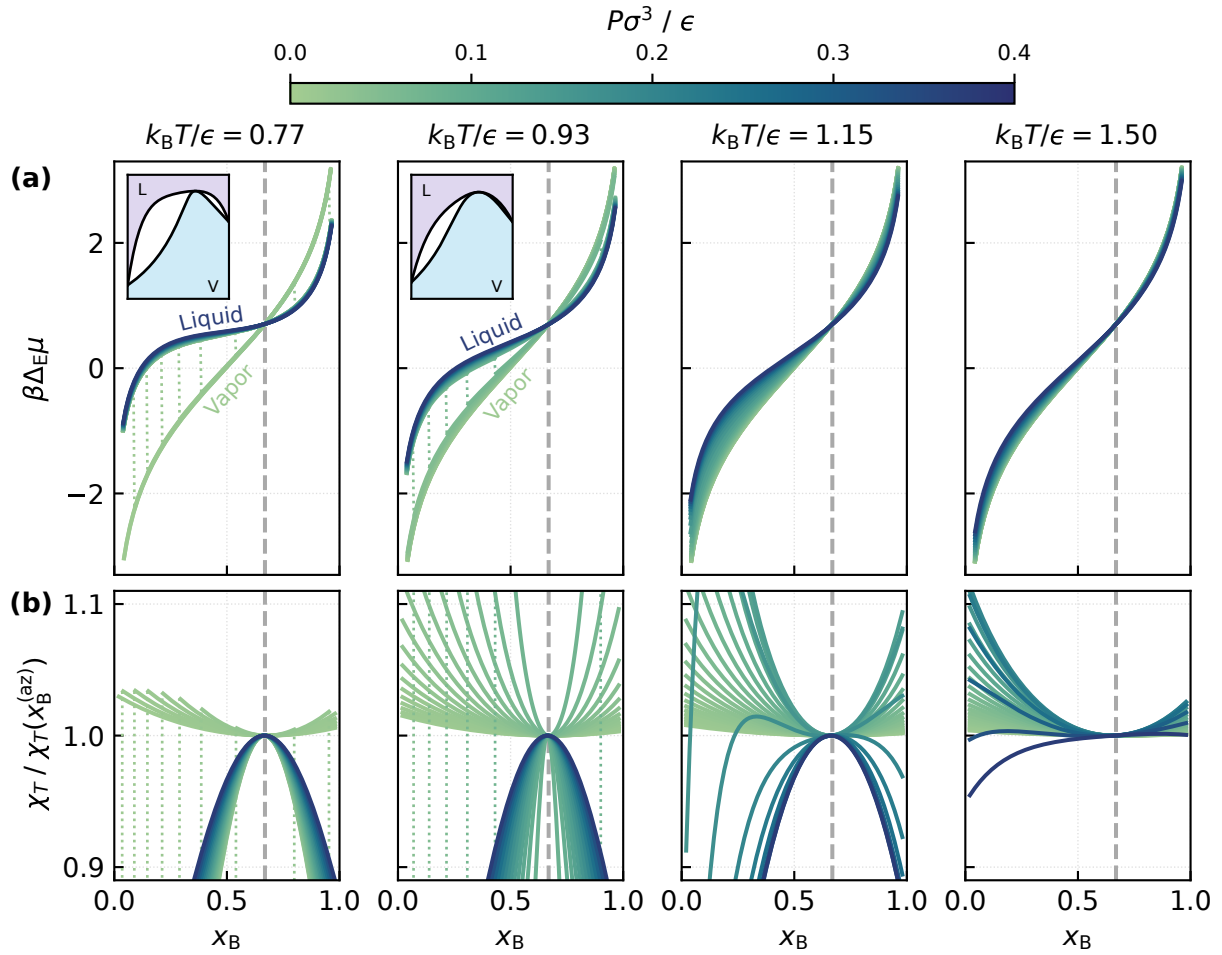


**Figure 3:** Bulk thermodynamic properties vs  $x_B$  for different  $P$  and  $T$ . From left to right, the temperatures correspond to  $T \ll T_c$ ,  $T \lesssim T_{\text{CAEP}} < T_c$ ,  $T > T_c$ , and  $T \gg T_c$ . (a) For subcritical temperatures,  $\Delta_E\mu$  collapses into liquid and vapor branches that cross at  $x_B \approx x_B^{(\text{az})}$ ; this crossing point persists at supercritical temperatures. The insets show schematic representations of the  $P$ - $x_B$  phase diagram at subcritical temperatures. (b) The isothermal compressibility is locally extremum at  $x_B \approx x_B^{(\text{az})}$  at all temperatures. In both (a) and (b), discontinuities representing liquid–vapor phase transitions are shown with dotted lines.

## V. THERMODYNAMIC ORIGIN AND CONTROL OF SELECTIVE ADSORPTION IN CONFINED AZEOTROPIC MIXTURES

For the pores that we have considered so far, i.e., those that interact with species A and B in the same manner, our analysis indicates that the bulk thermodynamics of the fluid mixture play an important role in determining selective adsorption under confinement. While the observations that the partial molar volumes of A and B are equal at the azeotropic composition, and  $x_B^{(\text{an})} \approx x_B^{(\text{az})}$ , are intriguing, they do not by themselves provide a clear mechanistic explanation of the observed adsorption behavior. More generally, there has been significant interest to understand the mechanisms of selective adsorption under confinement, especially when B assumes the role of a minority species dissolved in A, e.g., carbon dioxide in water; in such cases,  $S_B$  is often dubbed “oversolubility.” In this context, there has been much work discussing the roles of adsorption vs

confinement-induced changes on the solubility (see, e.g., Ref. 84 for a review). Here, we present a simple thermodynamic analysis that sheds light on the driving forces that underpin  $S_B$ . Anticipating the results that follow, we find that, in the thermodynamic sense,  $S_B$  is driven solely by adsorption.

Following standard treatments of the thermodynamics of confined fluids [29, 36], our starting point is the exact differential of the surface excess grand potential,

$$d\Omega^{(\text{ex})} = -2s\mathcal{A}dT - \mathcal{A} \sum_{\alpha} \Gamma_{\alpha} d\mu_{\alpha} + 2\gamma d\mathcal{A} - f_s \mathcal{A} dH, \quad (22)$$

where  $s$  is excess entropy per unit area,  $f_s$  is the solvation force,  $\gamma$  is the fluid–wall interfacial tension, and

$$\Gamma_{\alpha} = \int_{-H/2}^{H/2} dz (\rho_{\alpha}(z) - \bar{\rho}_{\alpha}) = N_{\alpha}/\mathcal{A} - \bar{\rho}_{\alpha}H, \quad (23)$$

is the adsorption of species  $\alpha$ . Note that, in this thermodynamic picture, there is a degree of flexibility in choosing

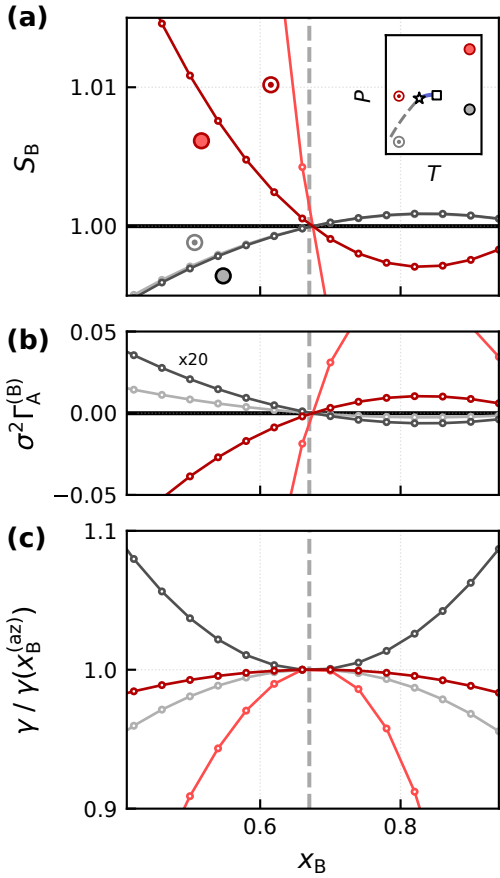


**Figure 4:** Coincidence of  $S_B = 1$ , vanishing relative adsorption, and extremal interfacial tension. (a)  $S_B$  vs  $x_B$  at the four different state points from Fig. 2 (and indicated in the inset). (b)  $\Gamma_A^{(B)}$  vs  $x_B$ , with results corresponding to low pressures (light and dark grey) multiplied by a factor 20 for clarity. (c) wall-fluid interfacial tension. The vertical dashed line indicates the azeotropic composition. All results corresponds to a slit pore with  $\beta\epsilon_{w,A} = \beta\epsilon_{w,B} = 2.0$  and  $L = 8\sigma$ .

$H$ , the separation between the two walls; to be consistent with  $N_\alpha$  used in Eq. 15,  $H$  should be large enough to encompass all particles in the slit pore; we discuss below how we choose  $H$  in practice. As  $\Omega^{(ex)} = 2\gamma\mathcal{A}$ , from Eq. 22 one can straightforwardly obtain the Gibbs adsorption equation for mixtures,

$$2d\gamma + 2sdT + \sum_\alpha \Gamma_\alpha d\mu_\alpha + f_s dH = 0, \quad (24)$$

from which it immediately follows that

$$\Gamma_\alpha = -2(\partial\gamma/\partial\mu_\alpha)_{\mu_{\eta\neq\alpha}, H, T}. \quad (25)$$

From the definitions of  $S_\alpha$  (Eq. 15) and  $\Gamma_\alpha$  (Eq. 23), we obtain

$$S_B = \frac{1}{x_B} \frac{\Gamma_B + \bar{\rho}_B H}{\Gamma_A + \Gamma_B + (\bar{\rho}_A + \bar{\rho}_B)H}, \quad (26)$$

This exact relation makes explicit that the adsorptions of species A and B are the key thermodynamic quantities gov-

erning the pore selectivity. Note that  $S_B$  is independent of definition of  $H$ . Given the flexibility afforded by this invariance, we choose  $H$  such that  $\Gamma_B = 0$  when  $S_B = 1$ ; this is only possible if  $\Gamma_A$  also vanishes. That is, the relative adsorption,

$$\Gamma_A^{(B)} = \Gamma_A - (\bar{\rho}_A/\bar{\rho}_B)\Gamma_B, \quad (27)$$

is zero at  $S_B = 1$ . This result is confirmed in Figs. 4a and 4b, where we show how  $S_B$  and  $\Gamma_A^{(B)}$ , respectively, vary with  $x_B$  at various different thermodynamic state points, for a slit pore with  $\beta\epsilon_{w,A} = \beta\epsilon_{w,B} = 2.0$  and  $L = 8\sigma$ .

The point at which the relative adsorption is zero defines the azeotropic composition [86–88]. For the liquid–vapor interface of a similar binary LJ mixture to that studied here, Telo da Gama and Evans [87] also reported that  $x_B^{(an)} \approx x_B^{(az)}$ , for which they provided a qualitative explanation: at low  $x_B$ , the vapor phase is relatively enriched in species B, leading to preferential adsorption of B; at  $x_B = x_B^{(az)}$ , the liquid and vapor phases have identical compositions and the adsorption vanishes; for high  $x_B$  the liquid becomes relatively richer in species B than the vapor, causing the adsorption to change sign. In other words, the sign of  $\Gamma_A^{(B)}$  is controlled by whether the bulk vapor or bulk liquid phase is enriched in species B.

Telo da Gama and Evans also found that the liquid–vapor surface tension is minimum at the azeotropic point. From Eq. 25, and using the Gibbs–Duhem relation, we find

$$\left( \frac{\partial\gamma}{\partial x_B} \right)_{H, P, T} = -\frac{1}{2} \left( \frac{\partial\mu_A}{\partial x_B} \right)_{P, T} \left[ \Gamma_A - \left( \frac{1-x_B}{x_B} \right) \Gamma_B \right]. \quad (28)$$

Evaluating at  $x_B = x_B^{(an)}$ , where  $\Gamma_A = \Gamma_B = 0$ , we have

$$\left( \frac{\partial\gamma}{\partial x_B} \right)_{H, P, T} \Big|_{x_B=x_B^{(an)}} = 0. \quad (29)$$

While this result is consistent with the minimum reported in Ref. 87, more generally, it states that the azeotropic point corresponds to a extremum in surface tension. This prediction is borne out by results from hyper-DFT; as seen in Fig. 4c,  $\gamma(x^{(an)})$  changes from a local minimum to a local maximum as the system traverses from high to low pressures.

The above arguments readily extend to cases where the relative wall affinity  $\Delta\epsilon_w = \epsilon_{w,B} - \epsilon_{w,A} \neq 0$ . Intuitively, we expect that changing varying  $\Delta\epsilon_w$  will change the pore selectivity, and the azeotropic point. This notion is confirmed in Figs. 5a, 5b, and 5c, where we respectively show how  $S_B$ ,  $\Gamma_A^{(B)}$ , and  $\gamma$  vary with  $x_B$ , with  $\beta\Delta\epsilon_w = \pm 0.2$ , for a system at  $k_B T/\epsilon = 0.77$ ,  $P\sigma^3/\epsilon = 0.0248$ , and  $L = 8\sigma$ . As expected, we see that  $S_B = 1$  and the azeotropic composition coincide. The results also appear consistent with a minimum in interfacial tension, albeit a shallow one. Due to this shallowness, we have performed fits to a fourth-order polynomial, constrained to be minimum at  $x_B^{(an)}$ , as shown by the solid black lines in Fig. 5c.

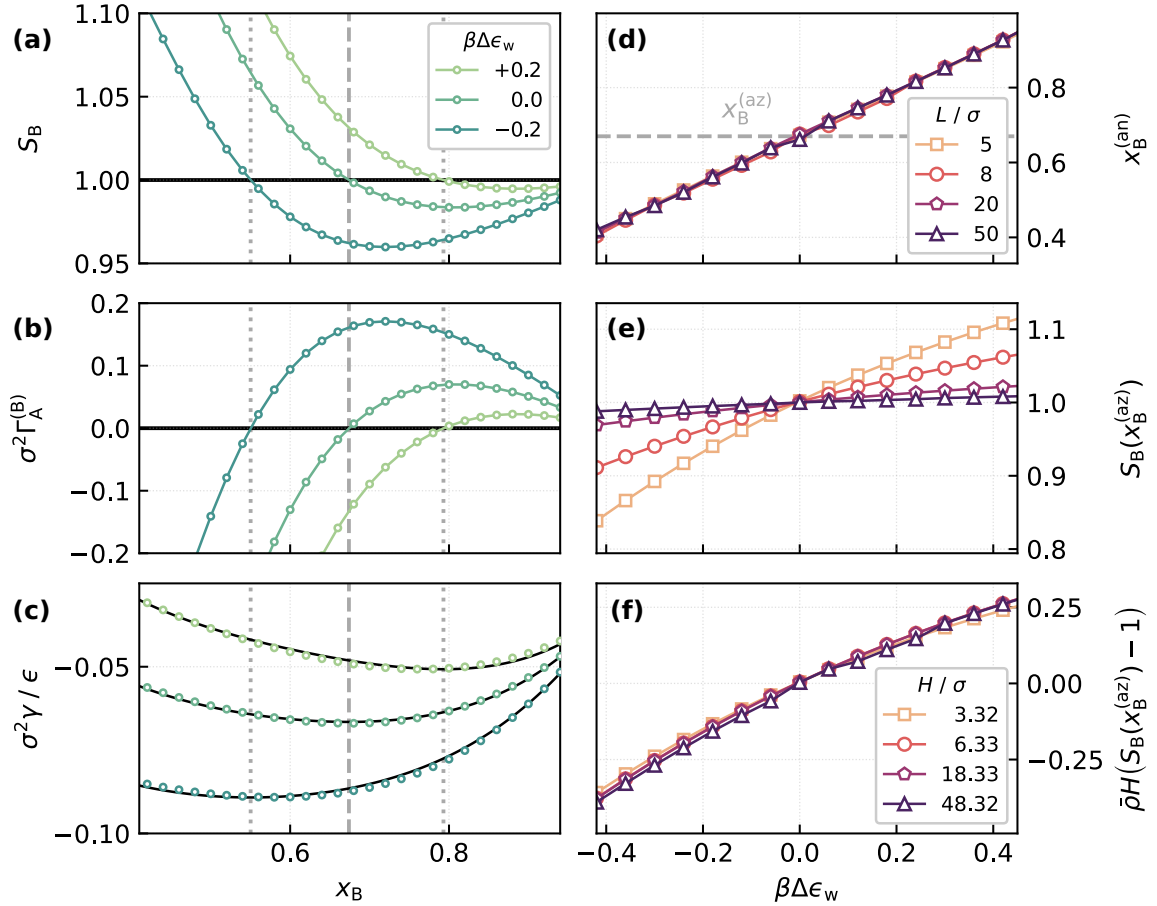


**Figure 5:** Effect of wall affinity,  $\Delta\epsilon_w = \epsilon_{w,B} - \epsilon_{w,A}$ , on the pore selectivity. In all cases,  $\beta\epsilon_{w,B} = 2.0$ . (a), (b), and (c) respectively show how  $S_B$ ,  $\Gamma_A^{(B)}$ , and  $\gamma$  vary with  $x_B$ . In all cases, we observe that  $S_B = 1$ ,  $\Gamma_A^{(B)} = 0$ , and a minimum in  $\gamma$  coincide. The vertical dashed and dotted lines indicate  $x_B^{(az)}$  and  $x_B^{(an)}$ , respectively. The solid black lines in (c) show fits to a fourth-order polynomial, constrained to be minimum at the azeotropic composition. Panel (d) shows how  $x_B^{(an)}$  varies with  $\beta\Delta\epsilon_w$  for different  $L$  (as indicated in the legend). (e)  $S_B(x_B^{(az)})$  vs  $\beta\Delta\epsilon_w$  for different widths of the slit pore. When rescaled according to Eq. 30 all data approximately collapse onto the same master curve, as seen in (f).

In Fig. 5d, we show how  $x^{(an)}$  varies with  $\beta\epsilon_w$  for different slit widths. To a very good approximation, the variation is linear, and insensitive to  $L$ . We interrogate this size-independence further by considering how selectivity varies with  $\Delta\epsilon_w$  within the context of the thermodynamic model presented above. As we have established that  $x_B^{(an)} \approx x_B^{(az)}$  when  $\Delta\epsilon_w = 0$ , it is a straightforward, though slightly tedious, matter to show that

$$\bar{\rho}H(S_B(x_B^{(az)}; \Delta\epsilon_w) - 1) = -\Delta\epsilon_w \left( \frac{\partial\Gamma_A^{(B)}(x_B^{(az)}; 0)}{\partial\Delta\epsilon_w} \right)_{H,P,T} . \quad (30)$$

In Fig. 5e we show how  $S_B(x_B^{(az)})$  varies with  $\Delta\epsilon_w$ , where we see that variation is nonlinear, which becomes more pronounced for smaller slit pores. In Fig. 5f, we plot the left hand side of Eq. 30 vs  $\Delta\epsilon_w$  for different slit widths. Strikingly, we observe that all data approximately collapse onto the same curve. This insensitivity to the slit width suggests that, even for systems barely large enough to accommodate

three layers of particles, the two interfaces of the slit pore essentially behave independently; in this case, down to the range of the wall–fluid interaction.

## VI. CONCLUSIONS AND OUTLOOK

In this study, we have extended the recently developed neural density functional theory to a binary mixture of Lennard–Jones particles that exhibits azeotropic phase behavior. In contrast to another recent neural functional theory study on mixtures [21], we have used machine learning to obtain an accurate representation of a *single component* repulsive reference system, and treated attractive interactions in a mean-field fashion. The mean-field approach that we adopt is rooted in hyperdensity functional theory [52, 53] and is similar in spirit to local molecular field theory derived by Weeks and co-workers [70–72]. Within this hyper-DFT framework, we have taken advantage of the fact that, when

known from other sources [66, 67], the bulk equation of state of the fluid can be integrated seamlessly, allowing us to focus applying density functional theory itself to inhomogeneous systems.

We have used this hyper-DFT framework to understand preferential adsorption of this binary fluid in a slit-pore geometry. In cases where the walls of the slit pore interact with both species of the fluid in the same manner, our numerical results indicate that when the reservoir is at its azeotropic composition, so too is the composition in the pore. Remarkably, this observation persists across a broad range of thermodynamic conditions, including far into the supercritical state. By analysing the bulk equation of state, we find that the azeotropic composition coincides with equal partial molar fractions of the constituent species, and a local extremum of the isothermal compressibility. Intriguing as these observations are, their generality to other fluids that exhibit azeotropy is an open question that warrants further investigation. For example, the system we have investigated has an azeotropic composition that is largely invariant with temperature and pressure; this does not generally hold, especially when the components have markedly different sizes [97].

To elucidate the mechanisms underlying pore selectivity, we have presented a thermodynamic description that connects selectivity directly to interfacial adsorption. This shows that the azeotropic composition, defined by vanishing relative adsorption, remains closely tied to the bulk azeotropic composition over a wide range of thermodynamic conditions, even under confinement. We show clearly that the relative adsorption of each species in the mixture is the relevant thermodynamic driving force, with the wall–fluid interfacial tension reaching an extremum at the azeotropic composition—a result that generalizes previous work on the liquid–vapor interface by Telo de Gama and Evans [87]. By analysing our numerical results within the context of this thermodynamic model, we found that the azeotropic composition shifts linearly with the relative affinity of the confining walls to the two species. Moreover, we found that the two interfaces of the slit pore act essentially independently down to remarkably small separations—a little over three molecular diameters—between the walls.

With machine learning techniques, it is now possible to accurately model systems of remarkable complexity—both in terms of their interactions and emergent phase behavior—using classical density functional theory. Here, we take “classical density functional theory” in a broad sense to encompass its recent extensions hyper-DFT [53] and meta-DFT [98]. Here, we have used hyper-DFT as a means to justify a mean-field treatment of attractive interactions, as well as to incorporate an established bulk equation of state into the framework. By learning the one-body direct correlation function once for a single-component system, which we then used as reference for a binary fluid, we have demonstrated a “train once, learn many” strategy as a proof-of-principle. For more complex systems, especially mixtures where particle sizes differ significantly, it may be prove fruitful to combine this strategy with meta-DFT, which aims to

learn the functional dependence on the interaction potential directly. Irrespective of the exact strategy that one adopts, it seems highly likely that classical density functional theory combined with machine learning will play an increasingly important role in understanding fluids relevant to physical chemistry.

## ACKNOWLEDGEMENTS

S.J.C. is Royal Society University Research Fellow at Durham University (Grant No. URF\R1\211144). A.T.B. acknowledges funding from the Oppenheimer Fund and Peterhouse College, University of Cambridge. This work made use of the the Hamilton HPC Service of Durham University and facilities of the N8 Centre of Excellence in Computationally Intensive Research (N8 CIR) provided and funded by the N8 research partnership and EPSRC (Grant No. EP/T022161/1). The Centre is coordinated by the Universities of Durham, Manchester, and York.

## DATA AVAILABILITY

Data and code supporting the findings of this study are openly available at <link to be inserted upon publication>.

## SUPPORTING INFORMATION

Supporting information includes additional results validating the accuracy of the mean-field neural hyper-DFT approach, comparison to standard mean-field cDFT, and additional calculations for other binary LJ mixtures.

## METHODS

**Generation of training data.** Following Ref. 19, 900 GCMC simulations using our own code available on Github (<https://github.com/annatbui/dielectrocapillarity-cdft>) or Zenodo [99] were performed for a single-component WCA fluid at temperatures  $k_B T/\epsilon = 1.0, 1.5$  and  $2.0$  with randomized chemical and external potentials. The chemical potentials were chosen from the range  $-10 \leq \beta\mu \leq 3$  and the external potentials had the form

$$V(z) = \sum_{n=1}^4 A_n \sin\left(\frac{2\pi n z}{\ell} + \Phi_n\right) + \sum_n V_n^{\text{lin}}(z)$$

where  $A_n$  were randomly chosen Fourier coefficients from a normal distribution of variance  $2.5(k_B T)^2$  and the phases  $\Phi_n$  were chosen uniformly between  $0$  and  $2\pi$ . The simulation box was cubic with length  $\ell = 10\sigma$  and periodic boundary

conditions were applied. The linear function  $V_n^{\text{lin}}(z)$  takes the form

$$V_n^{\text{lin}}(z) = V_{n,1} + \frac{(V_{n,2} - V_{n,1})(z - z_{n,1})}{(z_{n,2} - z_{n,1})}$$

for  $z_{n,1} < z < z_{n,2}$  and 0 otherwise, where  $z_{n,1}$  and  $z_{n,2}$  were uniformly chosen such that  $0 < z_{n,1} < z_{n,2} < \ell$ , and  $V_{n,1}$  and  $V_{n,2}$  were randomly chosen from a normal distribution with variance  $4(k_B T)^2$ . Each external potential had four sinusoidal segments, and between 1 and 5 linear segments. Half of the potentials had planar hard walls, where  $V(z) = \infty$  for  $z \leq z_w/2$  and  $z \geq \ell - z_w/2$ ;  $z_w$  was randomly chosen uniformly between  $1\sigma$  and  $3\sigma$ .

Each simulation was run for  $10^9$  steps, with equilibration for  $10^6$  steps. For each simulation, the planar density profile  $\rho(z)$  was obtained from a histogram of the positions of the particles, and  $c_R^{(1)}(z; [\rho], T)$  was obtained from numerical evaluation of the single component variant of Eq. 4. The total computation time for the generation of the entire training dataset is on the order of  $10^4$  CPU hours.

**Training the neural functional.** Our training procedure largely follows that of previous work [19–22]. A neural network was trained to represent  $c_R^{(1)}(z; [\rho], T)$ , implemented using Keras/Tensorflow with the standard Adam optimizer [100]. The input layers take in the temperature and the density in a window of size  $3\sigma$  around the location of interest, with spatial discretization  $\Delta z = 0.005\sigma$ . This was followed by two hidden layers of 32 nodes with softplus activation functions, and then the single-node output. The simulation dataset was split 3:1:1 for the training, validation, and test datasets, respectively. Data augmentation allowed the dou-

bling of the training data through mirroring. The model was trained for 100 epochs in batches of size 256 with the mean squared error as the loss function. The initial learning rate was 0.001, decreasing by 5% per epoch. The training was done on an NVIDIA GH200 Grace Hopper Superchip in under an hour.

**Using the neural functional.** Once the neural functional has been trained, combining with LMFT using Eq. 9 gives  $c^{(1)}(z; [\rho], T)$ . Minimization of the Euler-Lagrange equation to obtain density profiles is done self-consistently using a mixed Picard scheme, and typically takes around 2 minutes on a standard CPU (and faster on a GPU). For measurements of the pore selectivity, we first pick a bulk state point to obtain  $\mu_A$  and  $\mu_B$  from the PeTS EoS. We then perform a minimization to obtain the equilibrium density profiles of both species. To obtain surface tensions, we first use functional line integration to calculate  $\mathcal{F}_{\text{intr}}^{(\text{ex})}$ ,

$$\beta \mathcal{F}_{\text{intr}}^{(\text{ex})} / \mathcal{A} = - \int_0^1 d\lambda \sum_{\alpha} \int dz \rho_{\alpha}(z) c_{\alpha}^{(1)}(z; [\{\lambda \rho_{\alpha}\}], T),$$

obtain  $\beta \mathcal{F}_{\text{intr}}^{(\text{id})} / \mathcal{A} = \sum_{\alpha} \int dz \rho_{\alpha}(z) (\ln[\Lambda_{\alpha}^3 \rho_{\alpha}(z)] - 1)$ , and then calculate  $\Omega$  from Eq. 1. The surface tension is then obtained from

$$\gamma = \frac{\Omega + PV}{2\mathcal{A}},$$

where  $V = \mathcal{A}H$ , and  $P$  the bulk pressure. Overall we have performed approximately 6200 cDFT calculations, from which we directly obtain both equilibrium density profiles and free energies.

---

[1] D. S. Sholl and R. P. Lively, Seven chemical separations to change the world, *Nature* **532**, 435 (2016).

[2] H. Furukawa, K. E. Cordova, M. O’Keeffe, and O. M. Yaghi, The Chemistry and Applications of Metal-Organic Frameworks, *Science* **341**, 1230444 (2013).

[3] S. Capelo-Avilés, M. de Fez-Febré, S. R. G. Balestra, J. Cabezas-Giménez, R. Tomazini de Oliveira, I. I. Gallo Stampino, A. Vidal-Ferran, J. González-Cobos, V. Lillo, O. Fabelo, E. C. Escudero-Adán, L. R. Falvello, J. B. Parra, P. Rumori, G. Turnes Palomino, C. Palomino Cabello, S. Giancola, S. Calero, and J. R. Galán-Mascarós, Selective adsorption of CO<sub>2</sub> in TAMOF-1 for the separation of CO<sub>2</sub>/CH<sub>4</sub> gas mixtures, *Nat. Commun.* **16**, 3243 (2025).

[4] E. Barsotti, S. P. Tan, S. Saraji, M. Piri, and J.-H. Chen, A review on capillary condensation in nanoporous media: Implications for hydrocarbon recovery from tight reservoirs, *Fuel* **184**, 344 (2016).

[5] S. Clauzier, L. N. Ho, M. Pera-Titus, B. Coasne, and D. Farrusseng, Enhanced H<sub>2</sub> Uptake in Solvents Confined in Mesoporous Metal-Organic Framework, *J. Am. Chem. Soc.* **134**, 17369 (2012).

[6] S. Clauzier, L. N. Ho, M. Pera-Titus, D. Farrusseng, and B. Coasne, Enhanced H<sub>2</sub> Uptake of n-Alkanes Confined in Mesoporous Materials, *J. Phys. Chem. C* **118**, 10720 (2014).

[7] Q. Yang, P. Z. Sun, L. Fumagalli, Y. V. Stebunov, S. J. Haigh, Z. W. Zhou, I. V. Grigorjeva, F. C. Wang, and A. K. Geim, Capillary condensation under atomic-scale confinement, *Nature* **588**, 250 (2020).

[8] E. Khanjani, A. Fergola, J. A. López Martínez, S. Nazarnezhad, J. Casals Terre, S. L. Marasso, and B. Aghajanloo, Capillary microfluidics for diagnostic applications: Fundamentals, mechanisms, and capillarics, *Front. Lab Chip Technol.* **4** (2025).

[9] N. B. Wilding, Critical-point and coexistence-curve properties of the Lennard-Jones fluid: A finite-size scaling study, *Phys. Rev. E* **52**, 602 (1995).

[10] L. N. Ho, Y. Schuurman, D. Farrusseng, and B. Coasne, Solubility of Gases in Water Confined in Nanoporous Materials: ZSM-5, MCM-41, and MIL-100, *J. Phys. Chem. C* **119**, 21547 (2015).

[11] Y. Hu, H. Liangliang, Z. Shuangliang, L. Honglai, and K. E. Gubbins, Effect of confinement in nanoporous materials on the solubility of a supercritical gas, *Mol. Phys.* **114**, 3294 (2016).

[12] D. Fertig, H. Hasse, and S. Stephan, Molecular dynamics study of adsorption and wetting of mixtures of simple fluids

on planar walls, *J. Phys. Chem. C* **128**, 11340 (2024).

[13] X. Wang and B. Cheng, Integrating molecular dynamics simulations and experimental data for azeotrope predictions in binary mixtures, *J. Chem. Phys.* **161**, 034111 (2024).

[14] V. K. Shen and J. R. Errington, Determination of fluid-phase behavior using transition-matrix Monte Carlo: Binary Lennard-Jones mixtures, *J. Chem. Phys.* **122**, 064508 (2005).

[15] H. Kellay, D. Bonn, and J. Meunier, Prewetting in a binary liquid mixture, *Phys. Rev. Lett.* **71**, 2607 (1993).

[16] D. Bonn, H. Kellay, and G. H. Wegdam, Wetting and layering in critical binary fluid mixtures, *J. Chem. Phys.* **99**, 7115 (1993).

[17] A. T. Bui and S. J. Cox, A classical density functional theory for solvation across length scales, *J. Chem. Phys.* **161**, 104103 (2024).

[18] J. Wu and M. Gu, Perfecting Liquid-State Theories with Machine Intelligence, *J. Phys. Chem. Lett.* **14**, 10545 (2023).

[19] F. Sammüller, S. Hermann, D. De Las Heras, and M. Schmidt, Neural functional theory for inhomogeneous fluids: Fundamentals and applications, *Proc. Natl. Acad. Sci.* **120**, e2312484120 (2023).

[20] A. T. Bui and S. J. Cox, Learning Classical Density Functionals for Ionic Fluids, *Phys. Rev. Lett.* **134**, 148001 (2025).

[21] S. Robitschko, F. Sammüller, M. Schmidt, and R. Evans, Learning the bulk and interfacial physics of liquid–liquid phase separation with neural density functionals, *J. Chem. Phys.* **163**, 161101 (2025).

[22] F. Sammüller, M. Schmidt, and R. Evans, Neural Density Functional Theory of Liquid–Gas Phase Coexistence, *Phys. Rev. X* **15**, 011013 (2025).

[23] A. T. Bui and S. J. Cox, *Dielectrocapillarity for exquisite control of fluids* (2025), arXiv:2503.09855 [cond-mat].

[24] A. Ahmed and R. J. Sadus, Phase diagram of the Weeks-Chandler-Andersen potential from very low to high temperatures and pressures, *Phys. Rev. E* **80**, 061101 (2009).

[25] P. Cats, S. Kuipers, S. de Wind, R. van Damme, G. M. Coli, M. Dijkstra, and R. van Roij, Machine-learning free-energy functionals using density profiles from simulations, *APL Mater.* **9**, 031109 (2021).

[26] J. Yang, R. Pan, J. Sun, and J. Wu, High-Dimensional Operator Learning for Molecular Density Functional Theory, *J. Chem. Theory Comput.* **21**, 5905 (2025).

[27] S.-C. Lin, G. Martius, and M. Oettel, Analytical classical density functionals from an equation learning network, *J. Chem. Phys.* **152**, 021102 (2020).

[28] R. Evans, The nature of the liquid–vapour interface and other topics in the statistical mechanics of non-uniform, classical fluids, *Adv. Phys.* **28**, 143 (1979).

[29] J.-P. Hansen and I. R. McDonald, *Theory of Simple Liquids: With Applications to Soft Matter*, 4th ed. (Elsevier/AP, Amsterdam, 2013).

[30] J. Percus, Equilibrium state of a classical fluid of hard rods in an external field, *J. Stat. Phys.* **15**, 505 (1976).

[31] Y. Rosenfeld, Free-energy model for the inhomogeneous hard-sphere fluid mixture and density-functional theory of freezing, *Phys. Rev. Lett.* **63**, 980 (1989).

[32] R. Roth, Fundamental measure theory for hard-sphere mixtures: A review, *J. Phys. Condens. Matter* **22**, 063102 (2010).

[33] R. Roth, R. Evans, A. Lang, and G. Kahl, Fundamental measure theory for hard-sphere mixtures revisited: The White Bear version, *J. Phys. Condens. Matter* **14**, 12063 (2002).

[34] H. Hansen-Goos and R. Roth, Density functional theory for hard-sphere mixtures: The White Bear version mark II, *J. Phys. Condens. Matter* **18**, 8413 (2006).

[35] R. Evans, U. M. B. Marconi, and P. Tarazona, Fluids in narrow pores: Adsorption, capillary condensation, and critical points, *J. Chem. Phys.* **84**, 2376 (1986).

[36] R. Evans and U. Marini Bettolo Marconi, Phase equilibria and solvation forces for fluids confined between parallel walls, *J. Chem. Phys.* **86**, 7138 (1987).

[37] R. Evans, M. C. Stewart, and N. B. Wilding, Critical Drying of Liquids, *Phys. Rev. Lett.* **117**, 176102 (2016).

[38] R. Evans, M. C. Stewart, and N. B. Wilding, A unified description of hydrophilic and superhydrophobic surfaces in terms of the wetting and drying transitions of liquids, *Proc. Natl. Acad. Sci.* **116**, 23901 (2019).

[39] M. K. Coe, R. Evans, and N. B. Wilding, Density depletion and enhanced fluctuations in water near hydrophobic solutes: Identifying the underlying physics, *Phys. Rev. Lett.* **128**, 045501 (2022).

[40] Z. Tan and K. E. Gubbins, Selective adsorption of simple mixtures in slit pores: A model of methane–ethane mixtures in carbon, *J. Phys. Chem.* **96**, 845 (1992).

[41] E. Kierlik and M. L. Rosinberg, Density-functional theory for inhomogeneous fluids: Adsorption of binary mixtures, *Phys. Rev. A* **44**, 5025 (1991).

[42] E. Kierlik, Y. Fan, P. A. Monson, and M. L. Rosinberg, Liquid–liquid equilibrium in a slit pore: Monte Carlo simulation and mean field density functional theory, *J. Chem. Phys.* **102**, 3712 (1995).

[43] A. Taghizadeh and E. T. Keshavarzi, Population Inversion of Binary Lennard-Jones Mixtures in Nanoslit Pores (A Density Functional Theory Study), *J. Phys. Chem. B* **115**, 3551 (2011).

[44] S. Jiang, K. E. Gubbins, and P. B. Balbuena, Theory of Adsorption of Trace Components, *J. Phys. Chem.* **98**, 2403 (1994).

[45] C. Qiao, X. Yu, X. Song, T. Zhao, X. Xu, S. Zhao, and K. E. Gubbins, Enhancing Gas Solubility in Nanopores: A Combined Study Using Classical Density Functional Theory and Machine Learning, *Langmuir* **36**, 8527 (2020).

[46] A. R. Denton and N. W. Ashcroft, Weighted-density-functional theory of nonuniform fluid mixtures: Application to freezing of binary hard-sphere mixtures, *Phys. Rev. A* **42**, 7312 (1990).

[47] I. Napari, A. Laaksonen, V. Talanquer, and D. W. Oxtoby, A density functional study of liquid–liquid interfaces in partially miscible systems, *J. Chem. Phys.* **110**, 5906 (1999).

[48] P. H. van Konynenburg and R. L. Scott, Critical lines and phase equilibria in binary van der waals mixtures, *Philos. Trans. R. Soc., A* **298**, 495 (1980).

[49] L. Shang-Chun and M. Oettel, A classical density functional from machine learning and a convolutional neural network, *SciPost Phys.* **6**, 025 (2019).

[50] A. Simon, J. Weimar, G. Martius, and M. Oettel, Machine learning of a density functional for anisotropic patchy particles, *J. Chem. Theory Comput.* **20**, 1062 (2024).

[51] J. M. Rodgers and J. D. Weeks, Local molecular field theory for the treatment of electrostatics, *J. Phys. Condens. Matter* **20**, 494206 (2008).

[52] A. T. Bui and S. J. Cox, A first-principles approach to electromechanics in liquids, *J. Phys.: Condens. Matter* **37**,



Rev. Lett. **97**, 245702 (2006).

[92] V. Pipich and D. Schwahn, Densification of supercritical carbon dioxide accompanied by droplet formation when passing the Widom line, *Phys. Rev. Lett.* **120**, 145701 (2018).

[93] C. Cockrell, V. V. Brazhkin, and K. Trachenko, Transition in the supercritical state of matter: Review of experimental evidence, *Phys. Rep.* **941**, 1 (2021).

[94] G. G. Simeoni, T. Bryk, F. A. Gorelli, M. Krisch, G. Ruocco, M. Santoro, and T. Scopigno, The Widom line as the crossover between liquid-like and gas-like behaviour in supercritical fluids, *Nat. Phys.* **6**, 503 (2010).

[95] M. Raju, D. T. Banuti, P. C. Ma, and M. Ihme, Widom lines in binary mixtures of supercritical fluids, *Sci. Rep.* **7**, 3027 (2017).

[96] D. Saric, G. Guevara-Carrion, and J. Vrabec, Thermodynamics of supercritical carbon dioxide mixtures across the widom line, *Phys. Chem. Chem. Phys.* **24**, 28257 (2022).

[97] S. P. Pandit and D. A. Kofke, Evaluation of a locus of azeotropes by molecular simulation, *AIChE J.* **45**, 2237 (1999).

[98] S. M. Kampa, F. Sammüller, M. Schmidt, and R. Evans, Metadensity Functional Theory for Classical Fluids: Extracting the Pair Potential, *Phys. Rev. Lett.* **134**, 107301 (2025).

[99] A. T. Bui, GCMC with Gaussian truncated potentials, <https://doi.org/10.5281/zenodo.1837650> (2026).

[100] D. P. Kingma and J. Ba, Adam: A Method for Stochastic Optimization, in *3rd International Conference on Learning Representations, ICLR*, edited by Y. Bengio and Y. LeCun (San Diego, CA, USA, 2015).

# Supplementary information: The roles of bulk and surface thermodynamics in the selective adsorption of a confined azeotropic mixture

Katie L. Y. Zhou,<sup>1</sup> Anna T. Bui,<sup>2,1</sup> and Stephen J. Cox<sup>1, a)</sup>

<sup>1)</sup>Department of Chemistry, Durham University, South Road, Durham, DH1 3LE, United Kingdom

<sup>2)</sup>Yusuf Hamied Department of Chemistry, University of Cambridge, Lensfield Road, Cambridge, CB2 1EW, United Kingdom

(Dated: January 30, 2026)

## S1. COMPARISON TO SIMULATION AND STANDARD MEAN-FIELD THEORY

Archer and Evans previously established a connection between LMFT and traditional mean-field cDFT.<sup>1</sup> While similar to our formalism,  $\Delta\mu$  was identified as an integration constant, which for mixtures reads

$$\Delta\mu_\alpha = \sum_\eta \bar{\rho}_\eta \int d\mathbf{r}' u_{1,\alpha\eta}(|\mathbf{r} - \mathbf{r}'|). \quad (\text{S1})$$

In this section, we compare our hyper-DFT approach to the standard mean-field cDFT treatment. That is, we consider the above expression (Eq. S1) for  $\{\Delta\mu_\alpha\}$  together with a hard sphere (HS) reference; here we use the accurate neural functional from Ref. 2.

In Fig. S1 we show a comparison between our hyper-DFT framework and standard mean-field cDFT for capillary condensation (Fig. 1b in the main text), with a reservoir at  $k_B T/\epsilon = 0.77$ ,  $P\sigma^3/\epsilon = 0.020$ , and  $x_B = 0.78$ , which corresponds to the vapor state. Both approaches show the transition from a gas-like to liquid-like state when going from interaction strength  $\epsilon_{w,A} = \epsilon_{w,B} = 2.0k_B T$  to  $2.5k_B T$ . While both are in excellent agreement with GCMC simulation for the gas-like state, they begin to deviate for the higher-density liquid-like state. Minor discrepancies are observed for hyper-DFT, while the standard mean-field result overestimates the peaks in the density profiles.

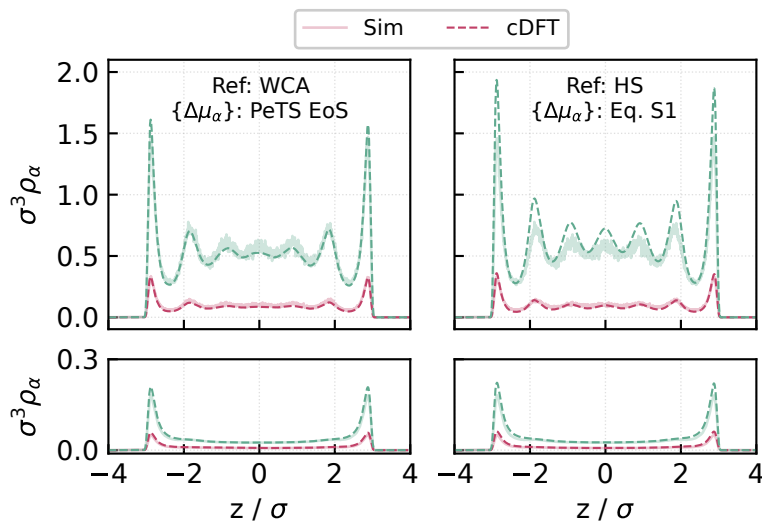


**Figure S1:** Comparison with the standard mean-field cDFT treatment for capillary condensation. Left: hyper-DFT, using a WCA reference and  $\{\Delta\mu_\alpha\}$  from the PeTS equation of state. Right: standard mean-field cDFT, using a HS reference and Eq. S1 for  $\{\Delta\mu_\alpha\}$ . Top row shows the condensed liquid state with  $\epsilon_{w,A} = \epsilon_{w,B} = 2.5 k_B T$ , while the bottom row shows the vapor state at  $\epsilon_{w,A} = \epsilon_{w,B} = 2.0 k_B T$ .

<sup>a)</sup>Electronic mail: [stephen.j.cox@durham.ac.uk](mailto:stephen.j.cox@durham.ac.uk)

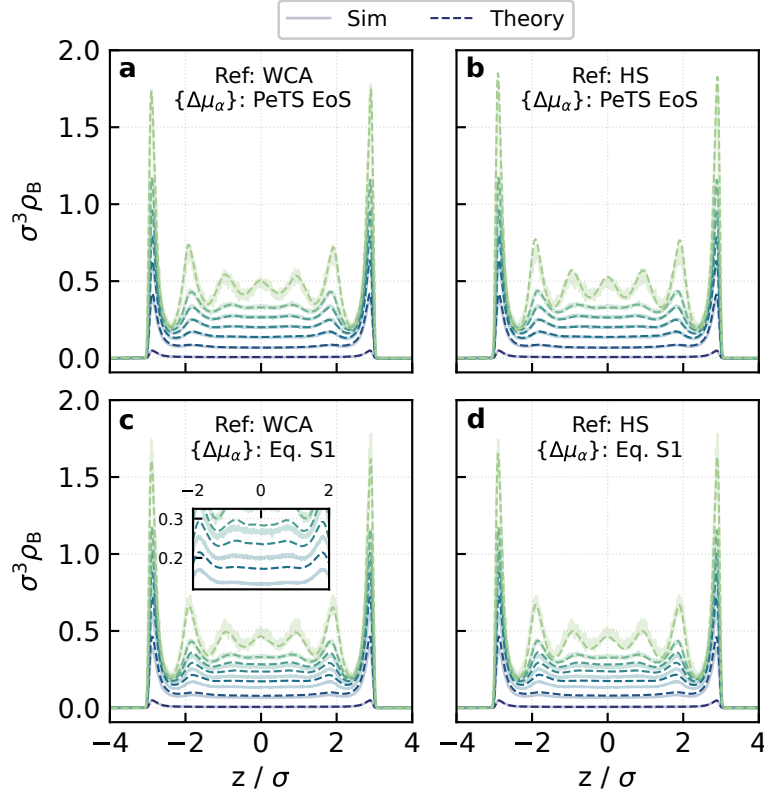


**Figure S2:** Comparison of reference systems and cDFT approaches at different bulk densities at supercritical conditions. (a) Hyper-DFT, using the WCA reference and the PeTS equation of state. (b) HS reference and the PeTS equation of state. (c) WCA reference and  $\{\Delta\mu_\alpha\}$  given by Eq. S1. (d) Standard mean-field cDFT, using a HS reference and  $\{\Delta\mu_\alpha\}$  given by Eq. S1.

In Fig. S2 we investigate the factors governing these differences in more detail, such as the reference system and the treatment of  $\{\Delta\mu_\alpha\}$ . The reservoir is now in a supercritical state at  $k_B T/\epsilon = 1.50$  and  $x_B = 0.66$ , with the total density varied between  $\bar{\rho} = 0.01$  to  $\bar{\rho} = 0.7$ . The two walls are separated by  $L = 8\sigma$  and interact with strength  $\epsilon_{w,A} = \epsilon_{w,B} = 2.0 k_B T$ . As observed in Fig. S2a, the hyper-DFT result, i.e., using the WCA reference and the PeTS equation of state for  $\{\Delta\mu_\alpha\}$ , results in excellent agreement with simulation across all densities. Switching to a HS reference in Fig. S2b results in similarly excellent agreement for most densities, though the system is over-structured at  $\bar{\rho} = 0.7$ . In Figs. S2c and S2d, we respectively use WCA and HS as reference, but  $\{\Delta\mu_\alpha\}$  is obtained with Eq. S1. While both reference systems show excellent agreement at the highest and lowest densities, neither obtains the correct bulk density at intermediate densities. This is in line with observations made with LMFT.<sup>3,4</sup>

Highlighting further the differences in bulk thermodynamics used by mean-field theory and the two reference systems, we present the binodal in Fig. S3 for the single-component truncated and shifted LJ fluid. The hyper-DFT approach, by construction, reproduces the same outputs as that from the PeTS equation of state. Fig. S3a shows an isotherm of the chemical potential as a function of bulk density at  $k_B T/\epsilon = 0.90$ . All approaches show a van der Waals loop. Performing a Maxwell construction on these isotherms gives the binodal in Fig. S3b. Comparing to simulation results from Ref. 5, the PeTS equation of state (and by extension, hyper-DFT) is the most accurate. The mean-field theories can accurately reproduce the vapor coexistence densities, though the WCA reference leads to an underestimate of the liquid densities. The HS reference, through cancellation of errors, results in accurate liquid densities below the critical temperature.

In addition to the errors with the coexistence densities, the mean-field approaches overestimate the critical temperature and underestimate the critical density. Near the critical temperature, an empirical fit can be made of the form<sup>6,7</sup>

$$\rho_\pm = a|T - T_c| \pm b|T - T_c|^\beta + \rho_c \quad (S2)$$

where  $\rho_+ = \rho^{(l)}$  and  $\rho_- = \rho^{(v)}$  are the liquid and vapor coexistence densities respectively,  $\rho_c$  is the critical

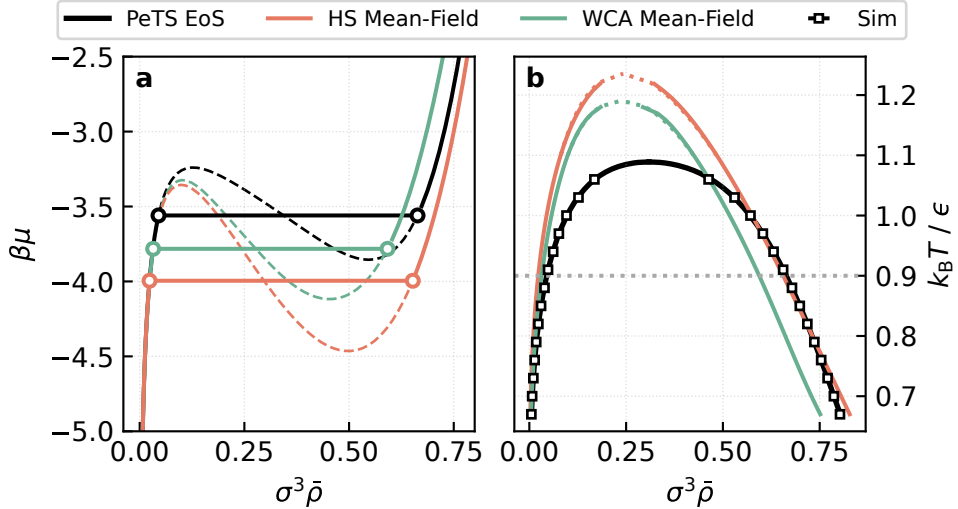


**Figure S3:** Bulk liquid–vapor coexistence for the single-component LJ fluid, comparing the EoS against the standard mean-field treatment with different reference systems. (a) The chemical potential as a function of bulk density at  $k_B T / \epsilon = 0.90$ , highlighted by the dotted grey line on the right. The coexistence densities obtained from Maxwell construction are shown by the circles. (b) The binodal obtained from Maxwell construction. Fits to the binodal to Eq. S2 are shown by the colored dotted lines. Simulation results are from Vrabec *et al.* in Ref. 5.

**Table S1:** Critical exponents extracted from the fits to the binodals (Eq. S2). The number in parentheses indicates the uncertainty in the last digit.

	HS Mean-Field	WCA Mean-Field	PeTS	Literature
$T_c$	1.236(1)	1.1909(6)	1.089 <sup>9</sup>	1.0779 <sup>5</sup>
$\rho_c$	0.2422(7)	0.2381(4)	0.3092 <sup>9</sup>	0.3190 <sup>5</sup>
$\beta$	0.500(3)	0.472(2)	0.350(2)	0.32630(22) <sup>8</sup>

density,  $\beta$  is the standard 3D Ising result,<sup>8</sup> and  $a$  and  $b$  are parameters to be fitted. Results are presented in Table S1. The PeTS equation of state returns values that are closest to those observed in literature.

## S2. RESULTS FOR OTHER SYSTEMS

One of the main benefits of using a single-component reference system is that it lends itself readily to a “train once, learn many” strategy. As further demonstration of this transferability, we show brief results in Fig. S4. Density profiles of truncated and shifted LJ binary mixtures with varying  $\epsilon_{BB}$  and  $\epsilon_{AB}$  are presented in Fig. S4a and compared to GCMC simulation. Parameters of the mixtures are summarized in Table S2. The bulk reservoir is at a supercritical state with  $k_B T / \epsilon = 1.50$ , with  $\beta \mu_A = \beta \mu_B = -2.0$ . The two walls interact with strength  $\epsilon_{w,A} = \epsilon_{w,B} = 2.0 k_B T$ . Excellent agreement of hyper-DFT to the simulation results can be seen. The same analysis with the pore selectivity conducted in the main paper can easily be extended to these other mixtures. In Fig. S4b, results are presented for the position of the azeotrope with  $\epsilon_{w,B} = 2.0 k_B T$  and varying  $\Delta \epsilon_w$  for systems confined in a slit of width  $L = 8\sigma$ . The bulk reservoir is at  $k_B T / \epsilon = 0.77$  and  $P\sigma^3 / \epsilon = 0.10$ , a bulk liquid for all systems. The interaction between unlike species is varied whilst  $\epsilon_{BB}$  is kept at  $0.9\epsilon$ . Like with the system studied in the main paper, we find that for the case of symmetric walls  $x_B^{(an)} \approx x_B^{(az)}$ . Varying the asymmetry of the wall potential leads to shifts in  $x_B^{(an)}$ .

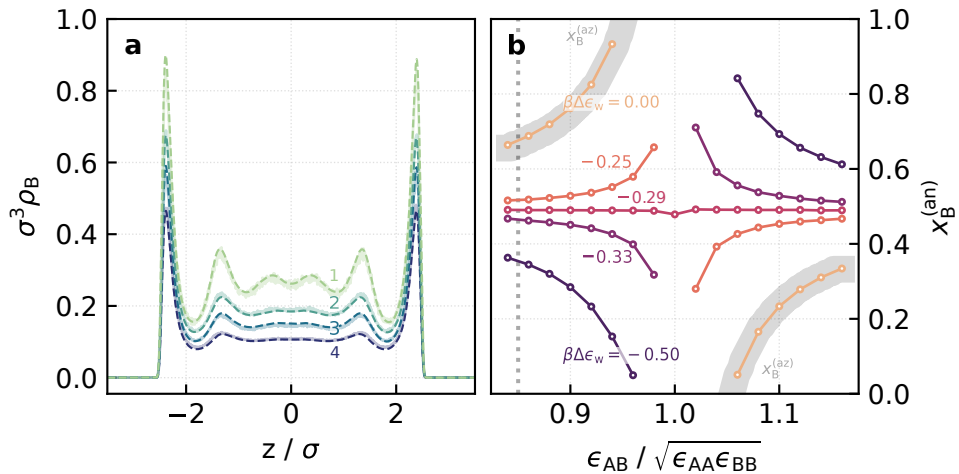


**Figure S4:** Varying  $\epsilon_{BB}$  and  $\epsilon_{AB}$  of binary LJ mixtures. (a) Density profiles of different binary LJ systems; the parameters are summarized in Table S2. Excellent agreement to GCMC simulations can be seen. (b) The position of the azeotrope ( $S_B = 1$ ) calculated for varying  $=\Delta\epsilon_w$  and  $\epsilon_{AB}$  for systems with  $\epsilon_{BB} = 0.9\epsilon$ . The shaded grey regions indicate the azeotropic composition, obtained from the PeTS equation of state.<sup>10,11</sup> The dotted line indicates the system studied in the main paper i.e.  $\epsilon_{AB} = 0.806\epsilon$ .

**Table S2:** Parameters of the LJ binary mixtures in Fig. S4a. Mixture 3 is the same as that studied in the main paper.

Mixture	$\epsilon_{BB} / \epsilon_{AA}$	$\epsilon_{AB} / \sqrt{\epsilon_{AA}\epsilon_{BB}}$
1	0.5	0.85
2	0.5	1.25
3	0.9	0.85
4	0.9	1.25

## REFERENCES

1. A. J. Archer and R. Evans, “Relationship between local molecular field theory and density functional theory for non-uniform liquids,” *J. Chem. Phys.* **138**, 014502 (2013).
2. F. Sammüller, S. Hermann, D. De Las Heras, and M. Schmidt, “Neural functional theory for inhomogeneous fluids: Fundamentals and applications,” *Proc. Natl. Acad. Sci.* **120**, e2312484120 (2023).
3. J. D. Weeks, K. Vollmayr, and K. Katsov, “Intermolecular forces and the structure of uniform and nonuniform fluids,” *Phys. Stat. Mech. Its Appl.* **244**, 461–475 (1997).
4. J. D. Weeks, K. Katsov, and K. Vollmayr, “Roles of Repulsive and Attractive Forces in Determining the Structure of Nonuniform Liquids: Generalized Mean Field Theory,” *Phys. Rev. Lett.* **81**, 4400–4403 (1998).

<sup>5</sup>J. Vrabec, G. K. Kedia, G. Fuchs, and H. Hasse, "Comprehensive study of the vapour–liquid coexistence of the truncated and shifted Lennard–Jones fluid including planar and spherical interface properties," *Mol. Phys.* **104**, 1509–1527 (2006).

<sup>6</sup>F. Sammüller, M. Schmidt, and R. Evans, "Neural Density Functional Theory of Liquid-Gas Phase Coexistence," *Phys. Rev. X* **15**, 011013 (2025).

<sup>7</sup>N. B. Wilding, "Critical-point and coexistence-curve properties of the Lennard-Jones fluid: A finite-size scaling study," *Phys. Rev. E* **52**, 602–611 (1995).

<sup>8</sup>A. M. Ferrenberg, J. Xu, and D. P. Landau, "Pushing the limits of Monte Carlo simulations for the three-dimensional Ising model," *Phys. Rev. E* **97**, 043301 (2018).

<sup>9</sup>S. Stephan, J. Liu, K. Langenbach, W. G. Chapman, and H. Hasse, "Vapor-Liquid Interface of the Lennard-Jones Truncated and Shifted Fluid: Comparison of Molecular Simulation, Density Gradient Theory, and Density Functional Theory," *J. Phys. Chem. C* **122**, 24705–24715 (2018).

<sup>10</sup>M. Heier, S. Stephan, J. Liu, W. G. Chapman, H. Hasse, and K. Langenbach, "Equation of state for the Lennard-Jones truncated and shifted fluid with a cut-off radius of  $2.5 \sigma$  based on perturbation theory and its applications to interfacial thermodynamics," *Mol. Phys.* **116**, 2083–2094 (2018).

<sup>11</sup>P. Rehner, G. Bauer, and J. Gross, "FeOs: An Open-Source Framework for Equations of State and Classical Density Functional Theory," *Ind. Eng. Chem. Res.* **62**, 5347–5357 (2023).